Tellus (1999), 51A-B, 45–58
Printed in UK – all rights reserved

TELLUS
ISSN 0280–6495
ISSN 0280–6509

Gravity waves in the mesosphere generated by tropospheric convention

By JAMES R. HOLTON* and M. JOAN ALEXANDER, *Department of Atmospheric Sciences, University of Washington, Box 351640, Seattle WA 98195, USA*

(Manuscript received 22 May 1998; in final form 3 August 1998)

ABSTRACT

The observed cold temperatures in the summer mesosphere are dynamically maintained primarily through upwelling induced in response to the action of a zonal drag force caused by the breaking of upward propagating gravity waves. Tropospheric convective storms are believed to be important sources of gravity waves in the summer mesosphere, but little is known about the characteristics of mesospheric gravity waves generated by convection. As a first attempt to model such waves a nonhydrostatic cloud-resolving numerical model is used to simulate a 2-dimensional squall line in a domain of width 2048 km and depth 90 km. The simulation produces a broad spectrum of convectively generated gravity waves. These propagate into the middle atmosphere, forming a fan-like pattern of waves with amplitudes increasing with height, and eventually reach breaking amplitudes in the mesosphere. The resultant mesospheric wave-breaking produces strong zonal forcing, which is eastward to the east of the storm center and westward to the west of the storm center. Breaking of upward propagating waves also generates high frequency downward propagating secondary waves of short horizontal wavelength, and long vertical wavelength. The secondary waves have only a small influence on the net vertical transfer of momentum, but produce a strong signature in perturbation vertical velocity, featuring alternating positive and negative interference with the primary upward propagating modes.

1. Introduction

Since the work of Leovy (1964) it has been known that the observed temperature structure of the mesosphere is dynamically produced through the action of a mean meridional circulation, which is maintained by a strong zonal drag force. This force draws air upward and equatorward in the summer hemisphere, and pushes it poleward and downward in the winter hemisphere. The resulting pattern of adiabatic cooling and heating maintains the summer mesospheric temperatures much below radiative equilibrium and the winter mesospheric temperatures much above radiative equilibrium. Some 25 years ago, Lindzen (1973) proposed that breaking gravity waves might provide the required zonal drag force in both the winter and the summer mesosphere. In the past two decades a growing body of research has accumulated in support of the view that momentum transfer by vertically propagating gravity waves is indeed the origin of this zonal drag (Fritts, 1989). It is thus essential that the effects of gravity wave drag be included in models of the circulation of the middle atmosphere, whether they be zonally symmetric (two-dimensional) models, or three-dimensional general circulation models (GCMs). Gravity wave drag is particularly crucial to an understanding of the cold summer polar mesopause, and the conditions that can produce noctilucent clouds (Lübken et al., 1996).

Lindzen (1981) introduced a simple scheme for parameterizing gravity wave drag in models of the

* Corresponding author.

zonal mean circulation. His scheme is based on the linear theory of monochromatic gravity waves. Variants of his scheme have been used in a number of studies of the zonally symmetric mesospheric circulation and transport (e.g. Garcia and Solomon, 1985; Holton, 1983; Holton and Schoeberl, 1988). Similar approaches have been used to parameterize the effects of orographically forced stationary gravity waves in general circulation models (McFarlane, 1987; Palmer et al., 1986) (see also the review by McLandress, 1998). Stationary gravity waves, however, cannot generally propagate to mesospheric altitudes in the summer hemisphere, and hence cannot provide the zonal forcing required to account for the cold summer polar mesopause.

In fact, observations indicate that there is a broad spectrum of gravity waves in the mesosphere, and that the largest momentum fluxes tend to be associated with high-frequency gravity waves (Fritts and Vincent, 1987). Such waves may be generated by a variety of processes, but among these, convective activity is likely the most important. For example, high frequency gravity waves attributed to convective sources are frequently observed in all-sky camera images of airglow from emission layers near the mesopause (Taylor and Hapgood, 1988; Swenson and Espy, 1995; Espy and Huppi, 1997).

Convective clouds occur in many forms, and the morphology of gravity waves generated by various types of convective cloud is not yet understood. In this work, which extends several previous studies (Alexander et al., 1995; Fovell et al., 1992; Holton and Durran, 1993), we examine gravity waves associated with a simulated two-dimensional midlatitude squall line. In our previous studies the upper boundary of the cloud model was placed in the middle stratosphere (30–35 km) and the focus of the model was on the generation of gravity waves in the troposphere and their propagation and mean-flow interactions in the first few scale heights above the tropopause. Here, we report an additional simulation in which the depth of the model domain has been extended to above the mesopause in order that the dynamics of the wave-breaking region of the mesosphere can be studied in detail. Prusa et al. (1996) have previously used a high resolution 2-dimensional model with a deep domain to simulate the vertical propagation of gravity waves generated in the troposphere, and their breakdown in the mesosphere. However, they did not simulate a convective storm. Rather, they attempted to mimic some effects of convection by specifying a simple time-dependent orography as a lower boundary condition. Their model also included no basic state wind shear. In the present work we use a nonhydrostatic cloud model to explicitly simulate a two-dimensional squall line, and study the propagation of convectively generated gravity waves into the mesosphere, their breakdown, generation of secondary waves, and mean flow forcing with realistic background shear.

As in our previous studies, we have neglected the rotation of the earth. The gravity waves generated by convection are primarily high frequency waves for which $|\omega| \gg |f|$, where ω is the wave frequency and f is the Coriolis parameter. Hence rotational effects are not significant for the wave propagation and wave breaking in the simulation. Rotation is expected to be of importance for the response of the mean flow to the wave forcing. However, the resulting geostrophic adjustment is inherently three-dimensional, and cannot be satisfactorily represented in a two-dimensional model.

2. Overview of the simulation

2.1. Model description

The storm simulation employed the nonhydrostatic cloud resolving model developed by Durran and Klemp (1983). This model was used in the two-dimensional squall line simulations reported by Fovell et al. (1992) and by Alexander et al. (1995). The reader is referred to the latter two papers for a description of the tropospheric characteristics of the squall-line simulation. For the present simulation the upper boundary of the model was moved to the 90 km level in order to simulate the behavior of convectively generated gravity waves throughout the depth of the mesosphere. Since waves propagate horizontally away from the source region as they propagate upward, it was also necessary to expand the horizontal domain to a width of 2048 km in order to keep most of the waves within the computational domain. The domain was specified to translate eastward at a speed of 16 m s^{-1}, which is approximately the speed of motion of the simulated squall line. Constant grid distances of 2.0 km in the

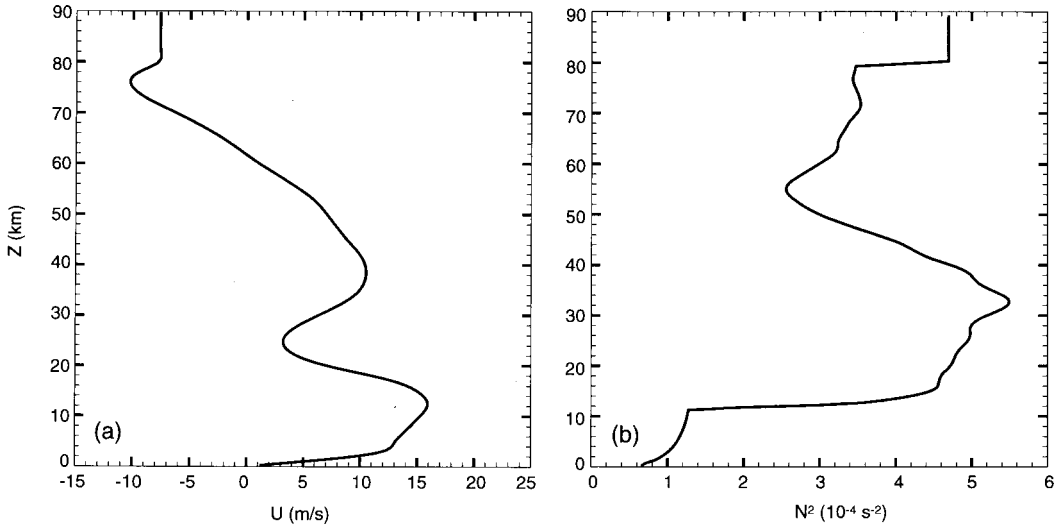

Fig. 1. (a) Initial profile of mean zonal wind relative to the ground in units of m s^{-1} (storm motion is approximately 16 m s^{-1} eastward). (b) Initial profile of buoyancy frequency squared (10^{-4} s^{-2}).

horizontal and 0.5 km in the vertical were employed in this simulation.

Radiation boundary conditions were imposed at both lateral and upper boundaries, as in Alexander et al. (1995). Since nearly 6 orders of magnitude in density and pressure are spanned by the deep computational domain, and wave amplitudes tend to vary with the inverse square root of density, vertically propagating gravity waves can attain very large velocity, pressure, and temperature perturbation amplitudes near the upper boundary. Although the radiation boundary condition at the upper boundary was very effective in preventing reflection, the large wave amplitudes near the upper boundary tended to produce numerical instability. In order to suppress this instability it proved necessary to include a Rayleigh friction "sponge layer", which extended from 78 to 90 km with a relaxation rate growing monotonically from zero at 78 km to a maximum of 10^{-3} s^{-1} at 90 km. Since the gravity waves reaching the mesopause region mostly have $|\omega| \gg 10^{-3}$ s^{-1}, the sponge layer has only a small effect on wave propagation. The sponge layer does, however, have a noticeable damping effect on the zonal flow forcing. Thus, only the region below 80 km was considered in most of the analyses reported below.

A weak fourth-order hyperdiffusion was applied to all prognostic fields in the horizontal and to the velocity and pressure fields in the vertical to prevent nonlinear instability. The hyperdiffusion substantially damped waves with horizontal wavelengths less than 10 km or vertical wavelengths less than 2 km. There was also a parameterized, Richardson-number-dependent, subgrid-scale mixing in the model (Durran and Klemp, 1983), which was important in the convective region of the troposphere and the wavebreaking region of the mesosphere.

The basic state in the troposphere (below 12 km) was the same as that used by Alexander et al. (1995), which in turn was based on that of Weisman and Klemp (1982). The zonal wind and potential temperature profiles were matched near the tropopause to a standard Northern Hemisphere midlatitude middle atmosphere climatology for April. Fig. 1 shows the resulting basic state profiles of mean zonal wind and buoyancy frequency squared. The buoyancy frequency has minima in the troposphere and mesosphere, rapid increases in height at the tropopause and the mesopause, and a more gentle decrease with height in the upper stratosphere. There is moderate easterly shear above the tropospheric jetstream, westerly shear in the midstratosphere, and easterly shear in the upper stratosphere and mesosphere. Since the squall line propagates eastward at about

16 m s^{-1}, all waves with eastward phase speeds relative to the squall line can propagate to the mesopause without encountering critical levels. Waves propagating westward relative to the squall line with phase speeds less than 13 m s^{-1} will encounter critical levels in the lower stratosphere, while those with westward phase speeds in the range 13–26 m s^{-1} will encounter critical levels in the mesosphere. Of the westward propagating waves excited by the storm, only those with phase speeds in excess of 26 m s^{-1} relative to the storm can propagate to the mesopause.

2.2. *Storm generated wave fields*

Convection is initiated by introducing a warm bubble with a 2 K temperature perturbation, centered at $x = 1024$ km and $z = 1.4$ km, with horizontal radius of 10 km and vertical radius of 1.4 km. During the first 2 h of the simulation a deep convective cloud develops and the tropospheric circulation gradually evolves into that of a typical squall line. A broad spectrum of gravity waves (zonal wavelengths $\sim$20 km to $\sim$200 km) is generated by the developing convection. Animations of the vertical velocity field show that high frequency, long vertical wavelength gravity waves with both positive and negative zonal phase velocities (relative to the translating coordinates) reach the mesopause within about 15 minutes of storm initiation. These waves have phase contours with zenith angles near 45° (approximately equal horizontal and vertical wavelengths). As the simulated squall line develops, waves of lower phase speed and larger zenith angle (hence, lower frequency and lower vertical group velocity) gradually reach the mesosphere, producing a fan like pattern of linear gravity waves by hour 2, as shown in Fig. 2a. Owing to the easterly mean wind shear in the mesosphere, the eastward waves have increasing intrinsic frequency as they propagate into the mesosphere, and hence their ray paths are refracted toward the vertical, while westward waves have decreasing intrinsic frequency and are refracted toward the horizontal. There is a slight decrease in vertical wavelength above 80 km caused by the increase in buoyancy frequency, but there is no evidence of reflection associated with the change in stability or the sponge layer above 78 km.

Shortly after hour 2 of the simulation the mesospheric waves to the east of the storm center begin to break in the layer between 65 and 80 km, and the wave pattern becomes much more complex as shown at hour 4 in Fig. 2b. In the eastern half of the domain in the mesosphere short horizontal wavelength waves have appeared with phase lines tilting opposite to the primary upward propagating waves, suggesting that downward propagating modes are generated by the wavebreaking. In the western half of the domain the filtering of waves by critical level absorption in the stratosphere leads to weaker wave amplitudes in the mesosphere, and significant wavebreaking in the mesosphere does not occur until near hour 6 of the simulation (Fig. 2c). In the later stages of the simulation the gravity waves generated by the storm become weaker, and the wave field spreads both eastward and westward in the mesosphere (Fig. 2d).

The contrast in the temporal development of wavebreaking between the eastern and western halves of the domain is illustrated by Fig. 3, which shows the time variations of the magnitude of the parameterized Richardson-number-dependent diffusion coefficient at the 75 km level averaged for the eastern and western halves of the domain, respectively. This parameter, which is a good measure of the intensity of wavebreaking, indicates that wavebreaking begins in the eastern half of the domain approximately 2 h earlier than in the western half of the domain.

2.3. *Zonal flow acceleration*

As discussed by Lindzen (1981), the breaking of zonally propagating gravity waves in the mesosphere leads to momentum flux convergence, and a zonal force. It is thus not surprising that wavebreaking in the simulation yields changes in the zonal flow in the mesosphere. Fig. 4 shows vertical profiles of the zonal flow at $t = 4$ h averaged over the whole domain and averaged separately for the eastern and western halves of the domain. At 4 h, wavebreaking is confined almost entirely to waves in the eastern half of the domain, propagating eastward relative to the storm. It is thus not surprising that the mean zonal wind has undergone a strong eastward acceleration in the eastern half of the domain, centered at the level of most vigorous wavebreaking near 75 km. There is, however, also a substantial eastward acceleration in

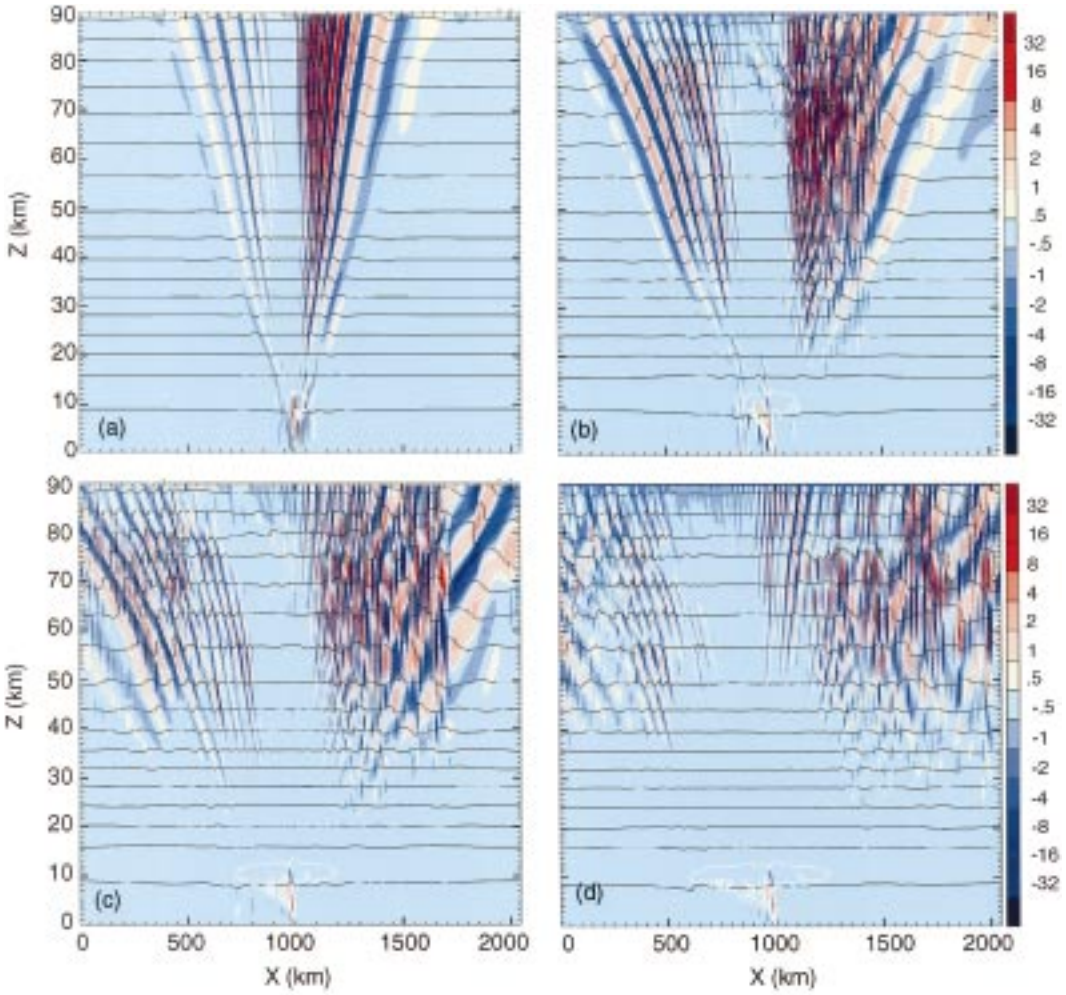

Fig. 2. Whole domain cross-sections (x increasing eastward) showing vertical velocity (background color with variable contour interval as shown by scales on right of each panel), log of potential temperature (thin solid black contours at 0.2 interval), and cloud outline (white contour) for selected times. Panels (a), (b), (c), and (d) correspond to hours 2, 4, 6, and 8 of the simulation, respectively.

the western half of the domain, indicating that there is a substantial nonlocal response to the zonal forcing. As explained by Durran (1995) a local wave-induced force generates pressure disturbances that propagate far from the region of forcing, leading to a highly nonlocal mean flow response.

Once wavebreaking begins in the western half of the domain, the zonal force and mean zonal wind response are significantly altered. Fig. 5 shows an 8 h time section at 75 km altitude of the average mean zonal flows for the eastern and western halves of the domain, and for the whole domain. Prior to the initiation of wave breaking at about 2 h the mean zonal wind is almost constant at its initial value. As wave breaking begins in the eastern half of the domain an eastward acceleration occurs, which is strongest in the eastern half of the domain. Between hours 4 and 6, as the amplitude of wavebreaking increases in the western part of the domain, there is a strong westward acceleration. Though strongest in the

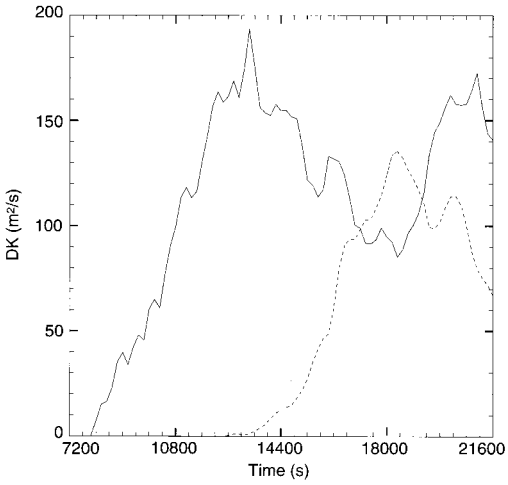

Fig. 3. Parameterized Richardson-number-dependent diffusion coefficient averaged over the eastern (solid line) and western (dashed line) halves of the computational domain at $z = 75$ km for the period from hour 2 to hour 6.

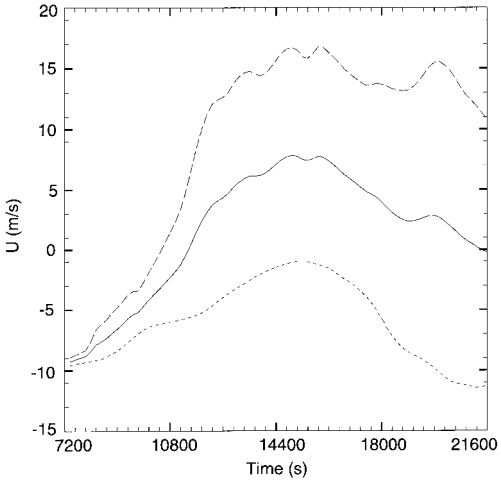

Fig. 5. Time variation of the zonal wind at $z = 75$ km for the period from hour 2 to hour 6 of the simulation. Solid line is the whole domain average, long dashes show eastern half of the domain, and short dashes show the western half of the domain.

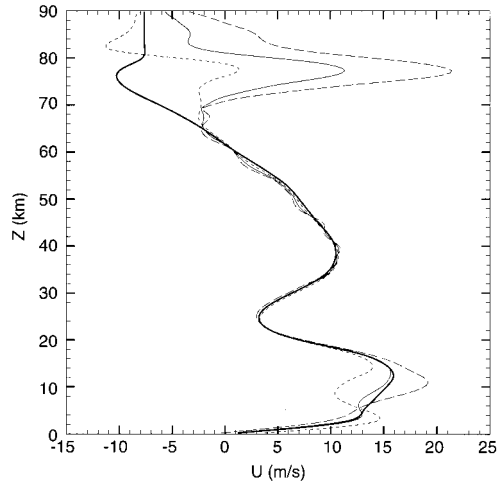

Fig. 4. Vertical profiles of the zonal wind at hour 4 averaged over the whole domain (thin solid), averaged over the eastern half of the domain (long dashes), and averaged over the western half of the domain (short dashes). The initial zonal wind profile is shown in the heavy solid line.

western half of the domain, this westward acceleration also has a nonlocal effect in the eastern part of the domain.

As a consequence of the zonal gradient in acceleration, the time averaged horizontal flow develops an x-dependence. In this 2-dimensional model the resulting divergence can only be balanced by convergence of a time-mean vertical mass flux. A vector plot of the time-mean (u, w) circulation for hours 5–6 is shown in Fig. 6. There is a strong divergence of the zonal velocity centered in the region $1000 < x < 1200$ km, which is balanced primarily by vertical motion east of $x = 1100$ km. In interpreting this figure it should be kept in mind that rotation is neglected in the simulation. In the atmosphere a geostrophic adjustment would occur (Zhu and Holton, 1987), and the divergent circulation in the vertical plane would likely be much smaller than in the simulation.

3. Spectral analysis

3.1. *Secondary waves*

Visual inspection of the longitude-height cross sections in Fig. 2 suggests that mesospheric wave-breaking produces downward propagating waves of short horizontal wavelength (~ 20 km) and long vertical wavelength (20–30 km), which are superposed on the primary upward propagating waves.

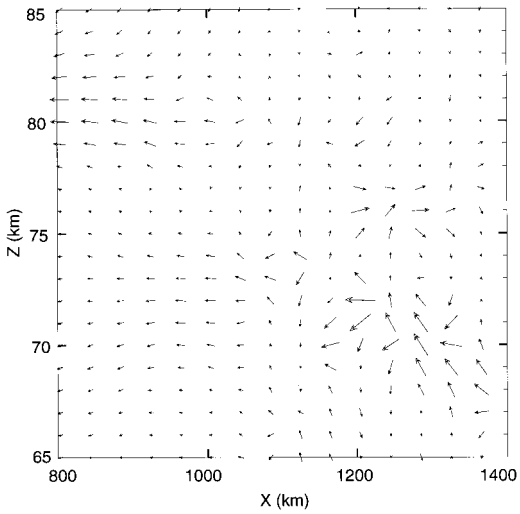

Fig. 6. Velocity vectors in the mesosphere ($65 < z < 85$ km) from 200 km west to 400 km east of the storm center shown at intervals of 1 km in the vertical and 40 km in the horizontal and time-averaged over hours 5–6. Vectors are scaled by the aspect ratio of the grid boxes. Maximum horizontal velocity is 30 m s^{-1} and maximum vertical velocity is 3 m s^{-1}.

These produce patterns of alternating constructive and destructive interference. In order to separate waves of upward and downward group velocity we have utilized a two-dimensional space × time Fourier analysis for the eastern half of the domain ($1024 \leqslant x \leqslant 2048$ km) using data fields saved at an interval of 180 s for the period from hour 2 to hour 8 of the simulation. Details of the spectral analysis method are given in Alexander et al. (1995).

The perturbation zonal and vertical velocities, $u'(x, t)$ and $w'(x, t)$ are fast Fourier transformed in x, and t to produce the transformed variables $U'(k, \omega)$ and $W'(k, \omega)$ where k and ω designate the zonal wavenumber and frequency, respectively. The cospectrum of (u', w') is given by $\mathrm{Co}(U'W') = \mathrm{Re}(U' \cdot W'^*)$, where W'^* is the complex conjugate of W'. Combinations of (k, ω) for which the cospectrum is positive correspond to upward propagating modes, and combinations for which the cospectrum is negative correspond to downward propagating modes. The cospectrum can thus be used to define masks M^+ and M^- for the upward and downward propagating modes, respectively. The mask M^+ has values of unity for (k, ω) values with positive cospectra and zero otherwise, while the mask M^- has values of unity for (k, ω) values with negative cospectra, and zero otherwise. Applying the inverse Fourier transform to the product of a Fourier transformed field variable and the M^+ mask yields the space–time distribution of the upward propagating mode for that field, while application of the M^- mask yields the downward propagating mode. Thus, for example, the horizontal and vertical velocity fields can be separated into upward and downward propagating fields $[u'_{\mathrm{up}}(x, t), w'_{\mathrm{up}}(x, t)]$ and $[u'_{\mathrm{down}}(x, t), w'_{\mathrm{down}}(x, t)]$, respectively. Note that masks applied in this way will lead to low-amplitude oscillations in the separated $(\,)_{\mathrm{up}}$ and $(\,)_{\mathrm{down}}$ fields transformed back to (x, t) space. These oscillations occur because of aliasing present in the Fourier spectrum. These aliasing effects result in oscillations that are ten times smaller in amplitude than the peak perturbations we are interested in, so they are only noticeable in regions where the true signal is very weak. In the wavebreaking region, this is only a minor effect.

The resulting distributions of vertical velocity for upward and downward modes at $t = 4$ h are shown in the two panels of Fig. 7 for the portion of the domain in which there is significant wavebreaking. Upward propagating modes clearly originate in the troposphere. But the downward propagating modes originate in the wavebreaking region near 75 km and propagate downward with long vertical wavelengths. The exact nature of the forcing for the secondary waves is not clear. There is, however, strong wave × wave interaction near the 75 km level, which generates harmonics of the primary waves, and in addition there is a strong heat source as a result of the parameterized Richardson number dependent vertical diffusion. The spatial distribution of the diffusion coefficient in the wavebreaking region east of the storm center at hour 4 is shown in Fig. 8. Large values of diffusion are associated with strong vertical mixing as is evident from the large spreading apart of the potential temperature contours in regions of large diffusion. The regions of enhanced diffusion in the 70–80 km layer have a characteristic horizontal scale similar to that of the secondary waves. It is plausible that the diffusion maxima act as heat and momentum "sources" for the secondary waves, and thus the horizontal scale of

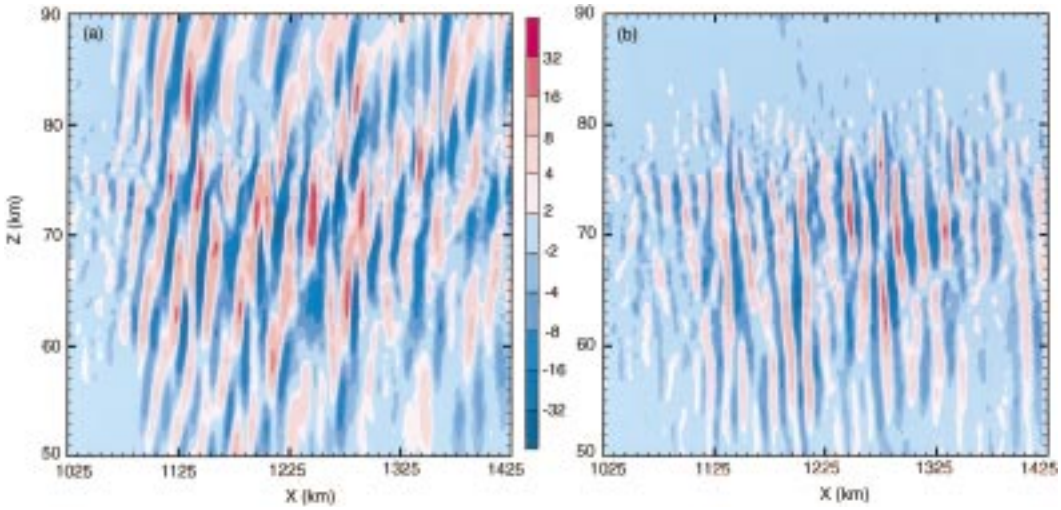

Fig. 7. Vertical velocity cross-sections for the upper portion of the eastern half of the domain at 4 h, corresponding to upward moving (a) and downward moving (b) wave components (background color contour intervals as in Fig. 2).

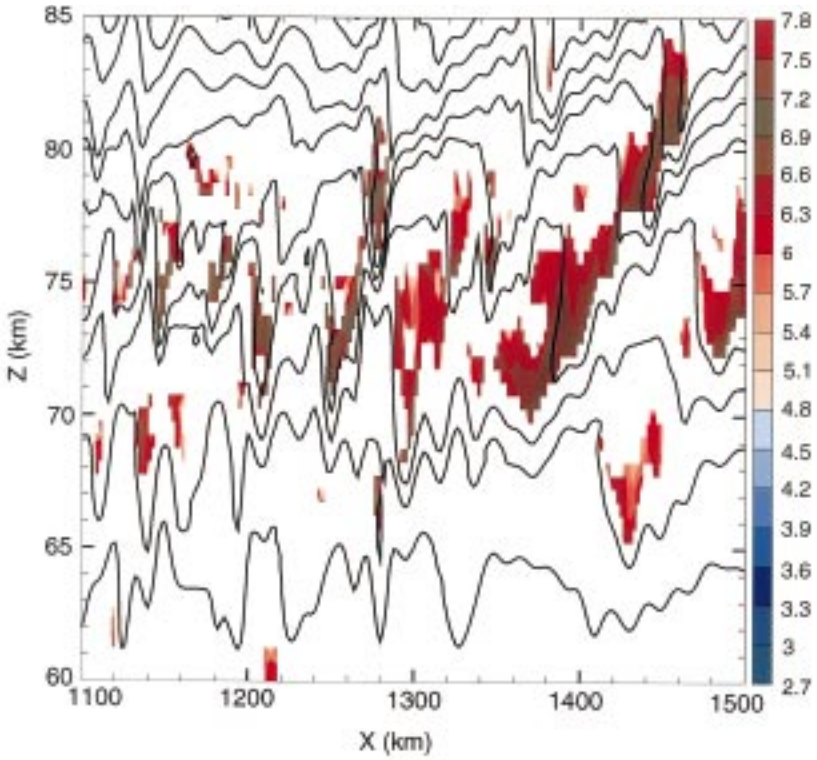

Fig. 8. Log of parameterized diffusion coefficient contoured at 0.3 interval (colorfill), and potential temperature (plotted from 3000 to 7500 K at interval of 500 K) at hour 4 in the mesosphere to the east of the storm center. Note that wavebreaking is strongest near 75 km.

the secondary waves is determined by the width of the wavebreaking regions of the primary waves.

Vertical velocity power spectral density versus horizontal wavelength, period, and zonal phase speed are shown separately for the up- and down-going waves in Fig. 9. The periods and phase speeds in Fig. 9 are "ground relative" values, those that would be seen by a ground-based observer. The spectra are averaged in height over the 60–70 km region, and the spectral analysis method inherently averages the power spectral density over the 2–8 h time period and the 1024–2048 km region of the domain. The downward propagating waves have much shorter periods and horizontal wavelengths on average than the upward propagating waves. The up- and down-going components have similar power at wavelengths of 15–25 km and periods shorter than 10 minutes, but the down-going wave spectra have an absence of power at the longer wavelengths and periods that dominate the spectra of up-going waves.

The generation of downward propagating secondary waves by wavebreaking in the middle atmosphere has been noted previously by Bacmeister and Schoeberl (1989) in a simulation of waves generated by flow over orography. However, in their case the downward propagating modes had horizontal wavelengths comparable to those of the primary upward propagating mode, rather than shorter as shown in Figs. 7 and 9. In addition, their downward propagating modes caused a substantial reduction in the net upward momentum flux, which as shown below, is not the case in the present simulation.

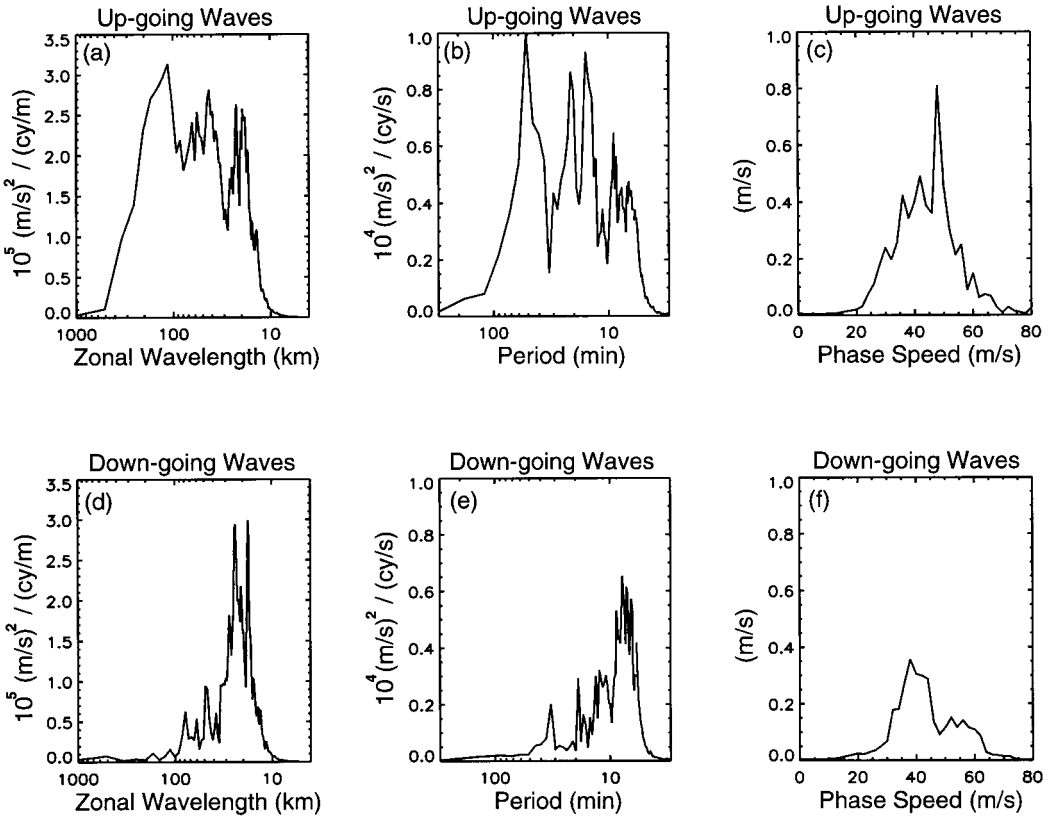

Fig. 9. Power spectra of the vertical velocity for the eastern half of the domain in the height and time intervals $60.25 < z < 69.75$ km and $7380 < t < 28\,800$ s, and separated into upgoing (top) and down going (bottom) waves. Spectra are plotted versus horizontal wavelength, period, and horizontal phase speed in the ground-relative frame, respectively.

3.2. Wave momentum fluxes

Fig. 10 shows vertical profiles of the momentum flux and resulting wave-driven horizontal force for waves in the eastern and western halves of the domain, respectively, averaged over the time period 7380–28 800 s of the simulation. These fluxes are computed as the integral over (k, ω) of the cospectrum $\mathrm{Co}(U'W')$ times the background density. Note that the westward momentum flux decreases rapidly in the lower stratosphere where waves propagating westward relative to the storm at low phase speeds encounter critical levels. The eastward momentum flux, on the other hand, decreases much more slowly with height, primarily as a result of waves propagating out of the domain. Owing to the exponential decrease of density with height, the wave-driven force

$$F_x = -\frac{1}{\rho}\frac{\partial(\rho\overline{u'w'})}{\partial z} \tag{1}$$

is concentrated in the mesosphere, and is dominated by the eastward force in the eastern half of the domain. In Fig. 11 the momentum flux and zonal force profiles in the eastern half of the domain are separated into the components associated with the upward and downward propagating waves, respectively. These are computed by integrating the product of density times the masked cospectra $M^+\,\mathrm{Co}(U'W')$ and $M^-\,\mathrm{Co}(U'W')$ for the eastward half of the domain giving the upward and downward fluxes respectively. The profile of momentum flux and zonal force associated with the upward mode is very close to the total. But, it is notable that the downward propagating mode contributes a significant westward force near $z =$ 75 km, the level where the secondary waves appear to originate, and that the momentum flux associated with the downward mode is nearly constant in height throughout much of the middle atmosphere.

The momentum flux analysis suggests a net wave-driven eastward force peaking in the 75–85 km region. Alexander (1996) computed the wave-driven force in the mesosphere associated with a nearly identical model storm, but using a linear ray tracing model to compute the wave propagation and a wavelet analysis to define wave packet dimensions. Dissipation in this linear analysis was estimated with a convective instability-based saturation condition on the wave amplitudes. The Alexander (1996) analysis predicted that the storm-generated waves propagat-

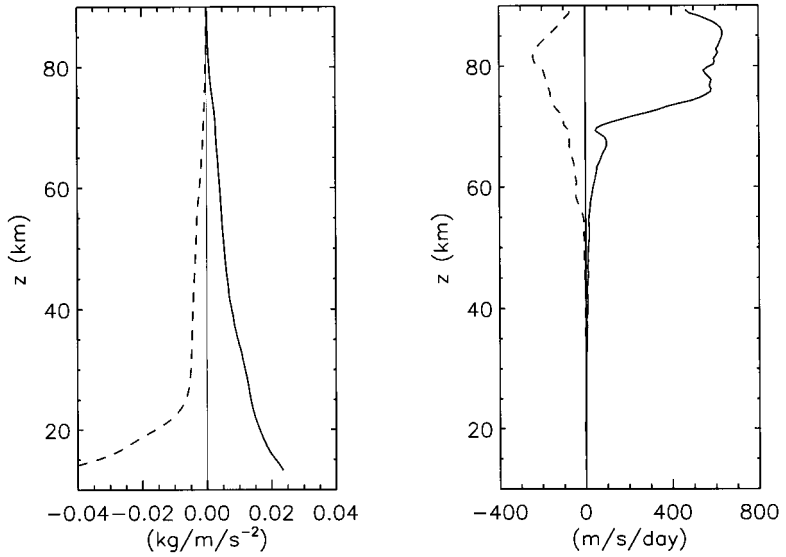

Fig. 10. Left panel: profiles of momentum flux, $\rho\overline{u'w'}$, in the eastern (solid) and western (dashed) halves of the domain. Right panel: wave-driven forces F_x (see eq. (1)) associated with the convergence of the momentum fluxes in panel (a). Eastern half (solid), western half (dashed). The momentum fluxes are computed from the cospectrum of u' and w' and represent averages over 1024 km in the horizontal and over the time period $7380 < t < 28\,800$ s.

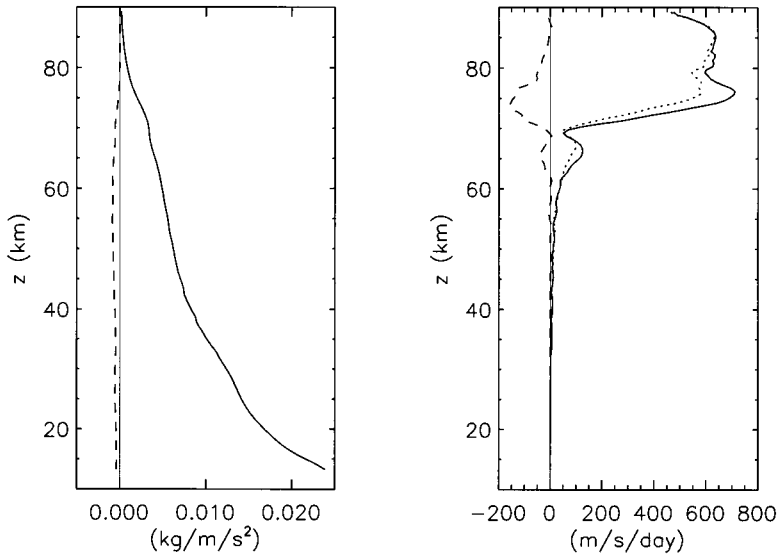

Fig. 11. Left panel: profiles of momentum flux, $\rho\overline{u'w'}$ (kg m^{-1} s^{-2}), in the eastern half of the domain carried by the upgoing (solid) and downgoing (dashed) waves. Right panel: wave-driven force (m s^{-1} day^{-1}) associated with the upgoing (solid) and downgoing (dashed) waves, and the sum of these (dotted). Note that the downgoing waves carry about 15–20% of the upgoing flux near 65 km.

ing through the same April zonal winds would drive an eastward force peaking near 80 km. The force when averaged over a day's time and over the 40 N latitude circle was predicted to be $\sim 12 \pm 5$ m/s/day. Computing the same zonal-mean daily averaged value from the results of the nonlinear model momentum budget above gives a peak of ~ 4 m/s/day. The generation of downward propagating secondary waves can explain approximately 20% of the discrepancy between these two estimates. The rest of the difference is likely explained by a combination of (1) wave propagation through the side boundaries, (2) weak but persistent dissipation acting in the nonlinear model at all altitudes, particularly affecting smaller horizontal wavelength waves, and (3) possible contributions to the forcing from waves with slow vertical group velocities that have not yet reached their breaking levels at the end of the present simulation. Each of these will tend to reduce the wave momentum flux convergence in the mesosphere in the nonlinear model.

4. Discussion

As shown in Fig. 2, wavebreaking in the mesosphere produces large upward and downward vertical displacements of potential temperature surfaces, thus producing layers with temperature inversions alternating with layers of enhanced lapse rate. Fig. 12 shows a vertical temperature profile through the breaking region east of the storm center

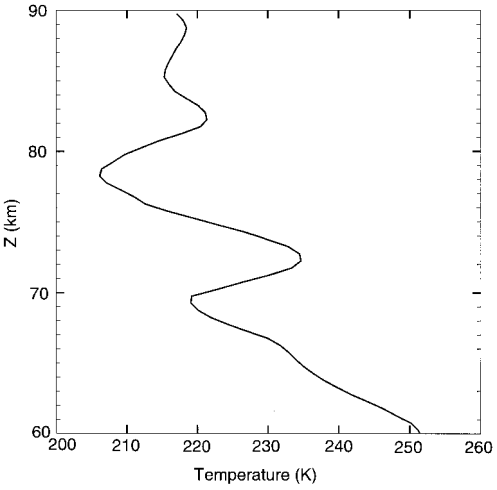

Fig. 12. Mesospheric temperature profile east of the storm center ($x = 1250$ km) at hour 6 of the simulation showing a strong temperature inversion near $z = 72$ km.

in which a strong temperature inversion layer occurs in the mesosphere. Hauchecorne et al. (1987) reported that such inversion layers are very frequently observed in temperature profiles of the winter mesosphere obtained by lidar in Southern France. They attributed the observed inversions to the breaking of upward propagating gravity waves and noted that such inversions are often capped by layers of enhanced mixing. Fig. 13 shows a cross section through the primary wavebreaking region of the temperature anomaly (defined as the local deviation from the initial zonally-uniform profile) and parameterized mixing coefficient averaged between hours 5–6. The section features regions of strong temperature inversion centered near 72 km, and regions of enhanced parameterized mixing coefficient just above the inversions.

The locations of mixing regions and temperature inversions are well correlated, supporting 1-dimensional model interpretations of these inversions as the direct consequence of turbulent heat transport (Whiteway et al., 1995). Warm anomalies range from 5–10 K with cold anomalies above and below. Mixing coefficients peak at 400–600 m^2/s. These results lend support to the hypothesis that spatial patterns in mesospheric temperature inversions observed by satellite (Leblanc et al., 1995) can be interpreted as describing spatial variations in gravity wave breaking in the mesosphere.

The intensity of mesospheric gravity waves in this simulation is probably greater than would be expected in the atmosphere for several reasons. Firstly, the simulation is two-dimensional whereas in reality, although the length scale along a squall line may greatly exceed the cross-line length scale, it is still short compared to the horizontal distance that longer period gravity waves travel to reach the mesosphere. Thus meridional dispersion of wave energy would be expected to occur as waves propagate upward into the mesosphere. In fact for most of the wave spectrum the tropospheric source will be closer to a point source rather than a line source. Secondly, the wavebreaking process itself will be highly three dimensional. Andreassen et al. (1994) have shown that the process of wavebreaking in three dimensions is much different from that in two dimensions. However, their study indicated that the qualitative aspects of the vertical distribution of momentum fluxes and mean flow acceleration appears to be captured in a 2-dimensional model.

Finally, though as stated earlier rotation will have little effect on the propagation or breaking

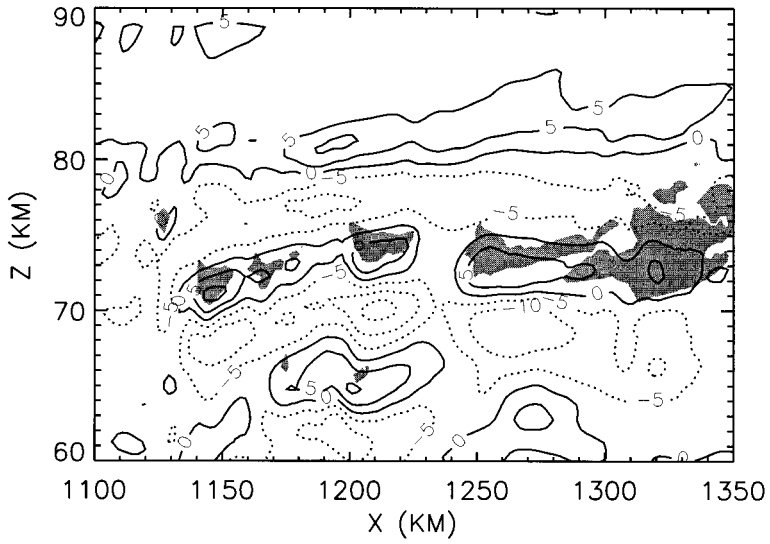

Fig. 13. Cross-section of temperature anomaly (defined as the difference from initial zonal mean conditions) in the wave breaking region averaged over hours 5–6 of the simulation. The contour interval is 5 K. Shading shows regions where the parameterized diffusion coefficient exceeds 200 $m^2 s^{-1}$.

of the high frequency gravity waves generated by the simulated storm, the geostrophic adjustment in the meridional direction that would accompany the zonal forcing produced by wavebreaking in a rotating system would modify the zonal flow response, and would lead to wave emission in the meridional direction. Study of these aspects of the problem will require a three-dimensional simulation.

5. Acknowledgments

We wish to thank Professor Dale Durran for advice on use of the convection model. This research was supported by the Physical Meteorology Program of the National Science Foundation under grant ATM-9322480 and by the National Aeronautics and Space Administration under NASA grant NAG-1-1803.

REFERENCES

Alexander, M. J. 1996. A simulated spectrum of convectively generated gravity waves: propagation from the tropopause to the mesopause, and effects on the middle atmosphere. *J. Geophys. Res.* **101**, 1571–1588.

Alexander, M. J., Holton, J. R. and Durran, D. R. 1995. The gravity wave response above deep convection in a squall line simulation. *J. Atmos. Sci.* **52**, 2212–2226.

Andreassen, Ø., Wasberg, C. E., Fritts, D. C. and Isler, J. R. 1994. Gravity wave breaking in two and three dimensions (1). Model description and comparison of two-dimensional evolutions. *J. Geophys. Res.* **99**, 8095–8108.

Bacmeister, J. T. and Schoeberl, M. R. 1989. Breakdown of vertically propagating two-dimensional gravity waves forced by orography. *J. Atmos. Sci.* **46**, 2109–2134.

Durran, D. R. 1995. Do breaking mountain waves decelerate the local mean flow? *J. Atmos. Sci.* **52**, 4010–4032.

Durran, D. R. and Klemp, J. B. 1983. A compressible model for the simulation of moist mountain waves. *Mon. Wea. Rev.* **111**, 2341–2361.

Espy, P. J. and Huppi, R. 1997. The intertropical convergence zone as a source of short-period gravity waves near the Equator. *J. Atmos. Sol-Terr. Phys.* **59**, 1665–1671.

Fovell, R., Durran, D. and Holton, J. R. 1992. Numerical simulations of convectively generated stratospheric gravity waves. *J. Atmos. Sci.* **49**, 1427–1442.

Fritts, D. C. 1989. A review of gravity wave saturation processes, effects, and variability in the middle atmosphere. *Pure Appl. Geophys.* **130**, 343–371.

Fritts, D. C. and Vincent, R. A. 1987. Mesospheric momentum flux studies at Adelaide, Australia: observations and a gravity wave-tidal interaction model. *J. Atmos. Sci.* **44**, 605–619.

Garcia, R. R. and Solomon, S. 1985. The effect of breaking gravity waves on the dynamics and chemical composition of the mesosphere and lower thermosphere. *J. Geophys. Res.* **90**, 3850–3868.

Hauchecorne, A., Chanin, M. L. and Wilson, R. 1987. Mesospheric temperature inversion and gravity wave breaking. *Geophys. Res. Letts.* **14**, 933–936.

Holton, J. R. 1983. The influence of gravity wave breaking on the general circulation of the middle atmosphere. *J. Atmos. Sci.* **40**, 2497–2507.

Holton, J. R. and Durran, D. 1993. Convectively generated stratospheric gravity waves: the role of mean wind shear. In: *Coupling processes in the lower and middle atmosphere,* (ed. Thrane, E. V. e. a.). Kluwer Academic Publishers, pp. 175–189.

Holton, J. R. and Schoeberl, M. R. 1988. The rôle of gravity wave generated advection and diffusion in the transport of tracers in the mesosphere. *J. Geophys. Res.* **93**, 11075–11082.

Leblanc, T., Hauchecorne, A., Chanin, M.-L., Rodgers, C., Taylor, F. and Livesey, N. 1995. Mesospheric temperature inversions as seen by ISAMS in December 1991. *Geophys. Res. Letts.* **22**, 1485–1488.

Leovy, C. B. 1964. Simple models of thermally driven mesospheric circulation. *J. Atmos. Sci.* **21**, 327–341.

Lindzen, R. S. 1973. Wave-mean flow interactions in the upper atmosphere. *Bound.-Layer Meteor.* **4**, 327–343.

Lindzen, R. S. 1981. Turbulence and stress owing to gravity wave and tidal breakdown. *J. Geophys. Res.* **86**, 9707–9714.

Lübken, F. J., Fricke, K. H. and Langer, M. 1996. Noctilucent clouds and the thermal structure near the Arctic mesopause in summer. *J. Geophys. Res.* **101**, 9489–9508.

McFarlane, N. A. 1987. The effect of orographically excited gravity wave drag on the general circulation of the lower stratosphere and troposphere. *J. Atmos. Sci.* **44**, 1775–1800.

McLandress, C. 1998. On the importance of gravity waves in the middle atmosphere and their parameterization in general circulation models. *J. Atmos. Terr. Phys.* **60**, accepted.

Palmer, T. N., Shutts, G. J. and Swinbank, R. 1986. Alleviation of a systematic westerly bias in general circulation and numerical weather prediction models through an orographic gravity wave drag parameterization. *Quart. J. Roy. Meteor. Soc.* **112**, 1001–10039.

Prusa, J. M., Smolarkiewicz, P. K. and Garcia, R. R. 1996. Propagation and breaking at high altitudes of gravity waves excited by tropospheric forcing. *J. Atmos. Sci.* **53**, 2186–2216.

Swenson, G. R. and Espy, P. J. 1995. Observations of

2-Dimensional Airglow Structure and Na Density from the ALOHA, October 9, 1993 "Storm Flight". *Geophys. Res. Letts.* **22**, 2845–2848.

Taylor, M. J. and Hapgood, M. A. 1988. The identification of a thunderstorm as a source of short period gravity waves in the upper atmospheric nightglow emission. *Planet. Space Sci.* **36**, 975–985.

Weisman, M. L. and Klemp, J. B. 1982. The dependence of numerically simulated convective storms on vertical wind shear and buoyancy. *Mon. Wea. Rev.* **110**, 504–520.

Whiteway, J. A., Carswell, A. I. and Ward, W. E. 1995. Mesospheric temperature inversions with overlying nearly adiabatic lapse rate: An indication of a well-mixed turbulent layer. *Geophys. Res. Letts.* **22**, 1201–1204.

Zhu, X. and Holton, J. R. 1987. Mean fields induced by local gravity-wave forcing in the middle atmosphere. *J. Atmos. Sci.* **44**, 2620–2630.